Inland and Near-Shore Water Profiles Derived from the High-Altitude Multiple Altimeter Beam Experimental Lidar (MABEL)

Authors: Jasinski, Michael F., Stoll, Jeremy D., Cook, William B., Ondrusek, Michael, Stengel, Eric, et al.

Source: Journal of Coastal Research, 76(sp1) : 44-55

Published By: Coastal Education and Research Foundation

URL: https://doi.org/10.2112/SI76-005

Journal of Coastal Research	SI	76	44–55	Coconut Creek, Florida	2016

Inland and Near-Shore Water Profiles Derived from the High-Altitude Multiple Altimeter Beam Experimental Lidar (MABEL)

Michael F. Jasinski[†], Jeremy D. Stoll[†‡], William B. Cook[§], Michael Ondrusek[ϕ], Eric Stengel[ϕ], and Kelly Brunt[ε††]

[†]Hydrological Sciences Laboratory
Code 617, NASA Goddard Space Flight Center
Greenbelt, MD 20771, U.S.A.

[‡]Science Systems and Applications, Inc.
Lanham, MD 20706, U.S.A.

[§]Mesoscale Atmospheric Processes Laboratory
Code 612, NASA Goddard Space Flight Center
Greenbelt, MD 20771, U.S.A.

[ϕ]Center for Satellite Applications and Research
NOAA National Environmental Satellite, Data, and Information Service
College Park, MD 20740, U.S.A.

[ε]Earth System Science Interdisciplinary Center
University of Maryland
College Park, MD 20740, U.S.A.

[††]Cryospheric Sciences Laboratory
Code 615, NASA Goddard Space Flight Center
Greenbelt, MD 20771, U.S.A.

www.cerf-jcr.org

www.JCRonline.org

ABSTRACT

Jasinski, M.; Stoll, J.; Cook, W.; Ondrusek, M.; Stengel, E., and Brunt, K., 2016. Inland and near-shore water profiles derived from the high-altitude Multiple Altimeter Beam Experiemental Lidar (MABEL). *In*: Brock, J.C.; Gesch, D.B.; Parrish, C.E.; Rogers, J.N., and Wright, C.W. (eds.), *Advances in Topobathymetric Mapping, Models, and Applications*. *Journal of Coastal Research*, Special Issue, No. 76, pp. 44–55. Coconut Creek (Florida), ISSN 0749-0208.

The Advanced Topographic Laser Altimeter System (ATLAS) on the Ice, Cloud, and Land Elevation Satellite (ICESat-2) mission is a six beam, low energy, high repetition rate, 532-nm laser transmitter with photon counting detectors. Although designed primarily for detecting height changes in ice caps, sea ice, and vegetation, the polar-orbiting satellite will observe global surface water during its designed three-year life span, including inland water bodies, coasts, and open oceans. In preparation for the mission, an ICESat-2 prototype, the Multiple Altimeter Beam Experimental Lidar (MABEL), was built and flown on high-altitude aircraft experiments over a range of inland and near-shore targets. The purpose was to test the ATLAS concept and to provide a database for developing an algorithm that detects along track surface water height and light penetration under a range of atmospheric and water conditions. The current analysis examines the datasets of three MABEL transects observed from 20 km above ground of coastal and inland waters conducted in 2012 and 2013. Transects ranged from about 2 to 12 km in length and included the middle Chesapeake Bay, the near-shore Atlantic coast at Virginia Beach, and Lake Mead. Results indicate MABEL's high capability for retrieving surface water height statistics with a mean height precision of approximately 5–7 cm per 100-m segment length. Profiles of attenuated subsurface backscatter, characterized using a Signal to Background Ratio written in Log10 base, or $LSBR_0$, were observed over a range of 1.3 to 9.3 m, depending on water clarity and atmospheric background. Results indicate that observable penetration depth, although primarily dependent on water properties, was greatest when the solar background rate was low. Near-shore bottom reflectance was detected only at the Lake Mead site down to a maximum of 10 m under a clear night sky and low turbidity of approximately 1.6 Nephelometric Turbidity Units (NTU). The overall results suggest that the feasibility of retrieving operational surface water height statistics from space-based photon counting systems such as ATLAS is very high for resolutions down to about 100 m, even in partly cloudy conditions. The capability to observe subsurface backscatter profiles is achievable but requires much longer transects of several hundreds of meters.

ADDITIONAL INDEX WORDS: *Lidar, inland water, coast, altimetry, ICESat-2, ATLAS, MABEL, photon counting, 532-nm, light penetration, subsurface backscatter, solar background, significant wave height.*

INTRODUCTION

Advancements in low energy (O[μJ]), high repetition rate (O[kHz]) lidar technology over the past several decades have generated strong interest in profiling surface waters from high altitude platforms, including orbiting satellites. Among the many improvements, perhaps the most useful has been the development of single photon counting detectors (Kraniak *et al*., 2010; McGill *et al*., 2002; Spinhirne, 1993). When coupled with a low energy, short pulse, laser transmitter, the technology offers the potential for improved performance and greater coverage of global terrestrial targets compared to traditional analog systems.

Background

Most lidar applications over the past several decades have focused on bathymetry, water surface height statistics, and biological activity using airborne scanning systems (Brock and Purkis, 2009; Guenther, 1985, 2007; Klemas, 2011). Bathymetric mapping generally includes coincident 532- and 1064-nm lidar, often in conjunction with hyperspectral imagery

DOI: 10.2112/SI76-005 received 7 July 2015; accepted in revision 30 April 2016.
*Corresponding author: michael.f.jasinski@nasa.gov

(Ackermann, 1999; Guenther, Tomas, and LaRocque, 1996; Krabill *et al*., 2002; Lillycrop, Pope, and Wozencraft, 2002) and high scan-rate systems such as the Experimental Advanced Airborne Research lidar (EAARL) (Bonisteel *et al*., 2009; McKean *et al*., 2009; Nayegandhi, Brock, and Wright, 2009; Wright *et al*., 2014) and the Scanning Hydrographic Operational Airborne Lidar Survey (SHOALS) (Irish and Lillycrop, 1999; Lillycrop, Irish, and Parson, 1997). Both high and low energy commercial systems are employed depending on environmental conditions. High energy systems that offer deep penetration but sparse pixel spacing include the Hawkeye II (Tulldahl and Wikstrom, 2012), the Laser Airborne Depth Sounder (LADS) MK3, and the Coastal Zone Mapping and Imaging Lidar (CZMIL) (Feygels *et al*., 2012; Fuchs and Mathur, 2010) systems. Low-altitude systems (< 3,000 m above ground) typically employ approximately 250-m swath widths 200–700-m above ground yielding vertical accuracies of 15 cm over 1 m spatial scale.

Low energy commercial systems suitable for shallow water and high spatial density observations include EAARL (Wright and Brock, 2002), Riegl VQ-880 series (Pfennigbauer *et al*., 2011), Optech's Aquarius (Pan *et al*., 2015), and the High-Resolution Quantum Lidar System (HRQLS) (Degnan *et al*., 2011). Example experimental low-energy photon counting systems include the low altitude Swath Imaging Multi-polarization Photon counting Lidar (SIMPL) (Dabney *et al*., 2010; Harding *et al*., 2011) and the high-altitude (20-km above ground) Cloud Physics Lidar (CPL) (McGill *et al.*, 2002). The photon counting systems, when combined with smaller telescopes and the elimination of automatic gain control, offer up to two orders of magnitude greater receiver performance than analog lidars (Krainak *et al.*, 2010).

Space-based retrievals of water properties have evolved over the past two decades. The first generation Geoscience Laser Altimeter System (GLAS) aboard ICESat-1 (Abshire *et al*., 2005) consisted of a single beam, low repetition rate (O[10^2]Hz), high pulse energy (O[10] mJ) lidar with an approximately 70-m footprint and along track spacing of about 170 m. Inland water observations were successfully explored with accuracies in the cm to decimeter range, and its height products were used in a number of both lake and river studies (Birkett *et al*., 2010; Calmant, Seyler, and Cretaux, 2008; Harding and Jasinski, 2004; Zhang *et al*., 2011a, 2011b). Future mission concepts, in addition to ICESat-2, that will employ photon counting detectors include the Lidar Surface Topography (LIST), the Active Sensing of CO_2 Emissions over Nights, Days, and Seasons (ASCENDS), and the Aerosols-Clouds-Ecosystem (ACE) missions.

In addition to range determination, the analysis of satellite-observed specular reflectance has allowed retrieval of additional water properties (Barrick, 1968; Bufton, Hoge, and Swift, 1983; Lancaster, Spinhirne, and Palm, 2005; Menzies, Tratt, and Hunt, 1998). Lancaster, Spinhirne, and Palm (2005) used the near-nadir ICESat GLAS reflectance to estimate ocean surface albedo. Menzies, Tratt, and Hunt (1998) were the first to examine sea surface directional reflectance and wind speed using the Lidar In-space Technology Experiment (LITE) instrument aboard the space shuttle. Hu *et al.* (2008) examined surface wind speed variability using NASA's Cloud-Aerosol Lidar with Orthogonal Polarization (CALIOP) backscatter data employing the Cox and Munk slope variance–wind speed relations. Several satellite lidar studies over oceans have focused on wind speed retrieval that relies on knowledge of backscatter distribution from wave slope facets (Hu *et al*., 2008; Lancaster, Spinhirne, and Palm, 2005; Menzies, Tratt, and Hunt, 1998). CALIOP observations over Tampa Bay were also used to investigate subsurface scattering (Barton and Jasinski, 2011).

The analysis of lidar returns from photon counting systems is, in many ways, similar to analysis using analog systems (Churnside, Naugolnykh, and Marchbanks, 2014; Guenther, 1985; Guenther, LaRocque, and Lillycrop, 1994). A principal difference is that, instead of analyzing a full waveform return from a single pixel illuminated by a high energy analog pulse, an equivalent, but not identical, histogram must first be generated from along track returns. The required track length depends on surface reflectance, atmospheric conditions, and solar background. In general, aggregations of at least 100 signal photons are sufficient for mean height analysis (Jasinski *et al*., 2015). For dark targets such as water, experience with MABEL indicates that about 0.5 to 1 signal photons per meter are returned (Jasinski *et al*., 2015). Range is measured from the time difference in between the laser pulse and the reflected light. Return intensity provides information on target characteristics. Factors affecting signal performance include Fresnel scattering from the water surface, water volume scattering and absorption, clouds, solar background, and bottom reflectance. While conceptually simple, execution requires precise measurements and timing. Optical water clarity is the most limiting factor for depth detection (Sinclair, 2008). In general, lidar technology can detect light down to about three times the Secchi depth (Estep, Lillycrop, and Parson, 1994; Sinclair, 1999) under ideal conditions. Recommended guidelines to achieve optimal performance include flying at night, low wind conditions, clear water, low altitude, and maximum sounding energy (Sinclair and Penley, 2007). Analysis of data from high-altitude aircraft platforms must also account for atmospheric scattering and delay and for aircraft pitch, roll, and yaw perturbations. Procedures to compare the various lidar waveform processing algorithms of different systems are available (Parrish *et al.*, 2011; White *et al*., 2011).

ICESat-2 ATLAS Mission

The soon-to-launch Advanced Topographic Laser Altimeter System (ATLAS) is the only instrument on the polar-orbiting Ice, Cloud, and Land Elevation Satellite (ICESat-2) mission. ICESat-2 is a Tier 1 mission recommended by the National Research Council (NRC, 2007). Its principal objectives are to quantify polar ice sheet contributions to sea level change and the linkages to climate conditions, quantify regional signatures of ice sheet changes, estimate sea ice thickness from freeboard measurements, and quantify and map vegetation height over a two-year period (Abdalati *et al.*, 2010). However, the ICESat2 mission will also develop inland water and ocean data products. The Inland Water data product, or ATL13, will consist of principally the mean and standard deviation of water surface height for ICESat-2 transects over global lakes, rivers, and near coastal regions.

ATLAS is configured as a six-beam laser altimeter utilizing a

high repetition rate (10k Hz), short pulse width, 532-nm laser transmitter with photon counting detectors, as shown in Figure 1. The spacing is configured to observe local cross slope within a beam pair and wide spatial coverage between the three sets of pairs. Each beam pair consists of a comparatively low energy (40 μJ) and strong energy (121 μJ) beam to better observe the full dynamic range of dark (water, vegetation) and bright (snow, ice) targets, respectively (McGill *et al*., 2013; Zwally *et al*., 2011).

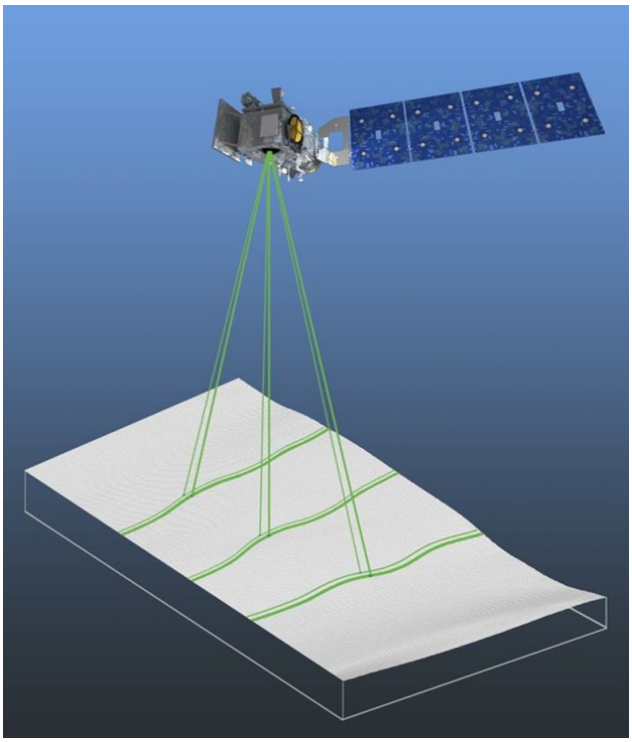

Figure 1. Schematic of ICESat-2 ATLAS six beam configuration. Credit: ICESat-2 Project Office.

ICESat-2/ATLAS is thus significantly different from its predecessor, ICESat/GLAS, which fired at a much lower rate (40 Hz) but employed ~80 mJ lasers for full waveform detection (Abshire *et al*., 2005; Schutz *et al*., 2005). In addition to the higher repeat frequency, ATLAS will offer near-continuous 0.70-m ground spacing with approximately 14-m footprints compared to GLAS's 170-m spacing and 70-m footprints. Each returned photon will be time-tagged with a vertical precision of approximately 30 cm, depending on surface and atmospheric characteristics (personal communication, Thomas Neumann, ICESat-2 Project Office). ATLAS also utilizes a narrower instrument field of view (FOV) to limit the observation of solar photons. The ATLAS system will thus provide higher measurement sensitivity with lower resource requirements. A summary of ATLAS parameters is shown in Table 1.

Table 1. *Summary comparison of the principal ATLAS and MABEL instrument parameters.*

Parameter	ATLAS	MABEL
Operational altitude	500 km	20 km
Wavelength	532 nm	532 and 1064 nm
Telescope diameter	0.8 m	0.127 m
Laser pulse repetition frequency	10 kHz	5–25 kHz
Laser pulse energy		
Strong beam	121 μJ	5–7 μJ per beam
Weak beam	30 μJ	5–7 μJ per beam
Mean Pulse Width (FWHM)	< 1.5 ns	< 2.0 ns
Laser footprint diameter	14 m	100 μrad (2 m)
Telescope field of view		210 μrad (4.2 m)
Swath width	3.3 km	Up to 1.05 km
Inclination	94 deg	N/A

An additional unique feature of ICESat-2 is its two orbit modes. Above approximately +/-65 deg latitude, ATLAS will operate in a repeat track mode over designated reference tracks similar to ICESat in order to obtain continuous time series of ice sheet change along those tracks. Below +/- 65 deg, however, ICESat-2 will systematically point left or right off the reference tracks in subsequent orbits in order to conduct a two-year global mapping of vegetation. Additional scheduled off-pointing is also planned to observe targets of opportunity and calibration/validation sites.

MABEL Prototype Instrument

The Multiple Altimeter Beam Experimental Lidar (MABEL) was built as a high-altitude prototype of the ATLAS instrument (McGill *et al*., 2013), but possessing additional beams and flexibility to test variations in the ICESat-2 concept. In this capacity it serves several purposes, including validation of ICESat models of instrument performance, evaluation of the photon counting system in the 532-nm band, providing experiment data over actual ICESat-2 targets, and development of retrieval algorithms of ICESat-2 data products. From 2012 through 2015, major flight experiments were conducted in Greenland, the east coast of the United States, the western United States, and Alaska. In all these experiments, MABEL was flown aboard either the ER-2 or Proteus Aircraft at 20 km or above 95% of the Earth's atmosphere. The high-altitude platform more realistically replicates the impact of clouds that ICESat-2 will encounter, and that will need to be addressed in the retrieval algorithms.

A summary comparison of the relevant ATLAS and MABEL instrument parameters is provided in Table 1. A unique feature of MABEL is that it possesses much flexibility in the configuration of several main lidar parameters. For example, it possesses up to 16 active channels at 532 nm and 8 at 1064 nm with changeable viewing angles, as shown in Figure 2. Laser repetition rate can be varied from 5 to 25 Hz. At 5 kHz and at an aircraft ground speed of 200 m/s, a pulse is thus emitted every 4 cm. Laser mean pulse width is 2 ns.

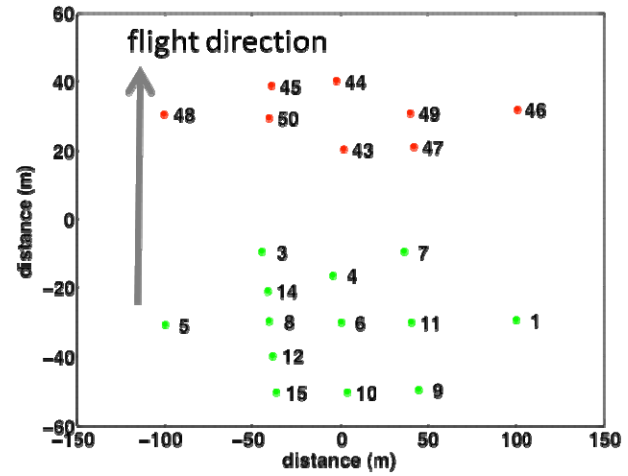

Figure 2. Typical MABEL beam configuration uses up to 16 active channels at 532 nm and 8 at 1064 nm.

Aim of This Study

The purpose of the present study is to analyze MABEL along track profiles of water surface height over inland and near-shore waters, and to evaluate what features can be derived from the ICESat-2/ATLAS instrument. The analysis is pertinent in the development of planned retrieval algorithms for the ICESat-2 Inland Water Body Height data product (ATL13). The primary ATL13 products are surface water height statistics including mean, standard deviation, and slope. However, they cannot be derived without considering additional processes that affect the retrieval, including the subsurface backscatter from the water column, the impact of a possible bottom signal in shallow areas, and meteorology. Analyses of the five cases reported herein serve to evaluate both the feasibility of the ATLAS photon counting lidar system for water surface profiling and to define the quality limits of the ATL13 data product.

METHODS

From 2012 through 2015, the ICESat-2 Project conducted several high-altitude MABEL flights aboard the ER-2 and Proteus aircrafts. These flights were planned as dedicated experiments for inland water targets recommended by the ICESat-2 Science Definition Team (SDT). Where available, flight lines were designed to pass over buoys that supported a number of *in situ* instruments that measured water surface height and water quality data.

Site Selection

Three sites from within the above experiments were selected to evaluate MABEL data over a range of inland and near-shore water bodies and operating conditions: i) Upper Chesapeake Bay near Gooses Reef on both September 22, 2012, at 00:56 UTC (evening local time) and September 25, 2013, at 16:51 UTC (noon local time), ii) Atlantic Ocean near Virginia Beach on September 20, 2013, at 22:23 UTC (early evening local time), and iii) Lake Mead on February 24, 2012, at 6:15 UTC (night local time).

The 2012 flights were flown aboard the ER-2 at an altitude of 20 km and an air speed of about 750 km/hr out of Dryden Air Force Base and the Wallops Flight Facility for the lake Mead and Chesapeake Bay cases, respectfully. The 2013 flights were flown aboard the Proteus out of Langley Air Force Base at about 12 km altitude and air speed of approximately 500 km/hr. Aircraft used are shown in Figure 3.

Figure 3. NASA ER-2 (a) and Proteus (b) aircraft used in the MABEL Experiments. Credits: NASA photo

Analyses

Once collected, data were first processed for individual photon geolocation by the ICESat Project Office. All MABEL data were grouped into granules of one-minute flight time. Accounting for the speed of the aircraft, each one-minute granule consists of about 99,000 photons covering a distance of about 12 km for ER-2 flights and 8 km for Proteus flights. Instantaneous photon height data are reported with respect to the WGS84 ellipsoid for all ice and land products. However, instantaneous heights were further converted in the case of inland water to orthometric height using the EGM96 Geoid.

Analysis of the data consisted of first plotting the along track heights of the individual MABEL photons to identify water surface, subsurface backscatter, and potential bottom reflectance. Several statistical parameters were then estimated including mean background rate, the rate of observed water surface photons (per meter of transect length), the observed mean geodetic and orthometric heights, the standard deviation of the water surface height and the MABEL subsurface attenuation coefficient. These are reported in Table 2 along with *in situ* observations when available.

Also computed was an expression of the vertical profile of MABEL's observable subsurface backscattered signal photons. This was formulated as the ratio of the depth-dependent signal photon density to mean background density, SBR(d), written (after Schroeder, 1999) as

$$SBR(d) = \frac{\rho_L(d)}{\rho_{SB} + \rho_{LB} + \rho_{DC}} \quad (1)$$

where $\rho_L(d)$ equals the observed lidar signal photon density (m^{-2}) as a function of depth, d, and the denominator represents mean sum of all background noise densities (m^{-2}) including solar background, ρ_{SB}, lidar background, ρ_{LB}, and dead count, ρ_{DC}. Mean background density, constant throughout the vertical column, was computed as the mean number of photon counts in

the atmosphere above the water surface, per meter depth per meter transect (m^{-2}). During daytime, the background consists mostly of solar backscatter. At night, the background density drops significantly and is primarily due to lidar backscatter.

Table 2. *Summary parameters of the MABEL experiments.*

FLIGHT DESCRIPTIONS						
Site		Ches Bay	Ches Bay (mod bckgr)	Ches Bay (low bckgr)	VA Beach	Lake Mead
Year	-	2012	2013	2013	2013	2012
Date	-	Sep-22	Sep-25	Sep-25	Sep-20	Feb-24
Time	UTC	00:56-57	16:51-52	16:51-52	22:23-24	06:15-17
Local Time	-	20:56-57	12:51-52	12:51-52	18:23-24	22:15-17
IN-SITU OBSERVATIONS						
Sky Condition[a]	-	Clear	Partly Cloudy	Mostly Clear	Mostly Clear	Mostly Clear
Wind Speed	m/s	5.4[b]	3.7[b]	3.7[b]	4.2[d]	8.5[e]
Wind Direction	Deg	162[b]	41[b]	41[b]	93[d]	27[e]
Turbidity	NTU	3.9[c]	2.9[b]	2.9[b]	2.2[d]	1.6[f]
Mean Water Surface	m	-	-	-	-	345.5[g]
Signif. Wave Ht[j]	m	0.35	0.17	0.17	0.58	-
K_{532}, Diff. Attn. Coef.	m^{-1}	-	0.45[p]	0.52[p]	-	-
DERIVED WATER CHARACTERISTICS FROM MABEL OBSERVATIONS						
Background Rate[m]	m^{-2}	0.00002	0.011	0.0053	0.0003	0.00008
Water Signal Rate[n]	m^{-2}	0.36	0.56	2.20	0.41	2.9
$LSBR_0$ Depth[k]	m	-6.8	-1.3	-3.7	-9.3	-9.2
Water Surface St Dev[l]	m	0.11	0.088	0.065	0.21	0.14
Mean Geodetic Ht[h]	m	-36.8	-40.0	-40.0	-43.2	315.9
Mean Orthom Ht[i]	m	-1.4	-4.6	-4.6	-3.6	344.8
Height Precision	cm	5.0	4.0	2.0	4.7	1.8
α_{5332}, Subs. Attn. Coef.	m^{-1}	0.69	0.91	0.56	0.55	0.40
α_{5332} x $LSBR_0$ (mean = 3.3)	-	4.7	1.3	2.1	5.1	3.4

[a]Based on MABEL-aircraft pilot mission notes
[b]Chesapeake Bay Interpretive Buoy System station 44062 (Gooses Reef, MD)
[c]Chesapeake Bay Interpretive Buoy System (Interpolation between Annapolis, MD / Potomac, MD)
[d]NOAA station CHYV2 (Cape Henry, VA)
[e]USGS Nevada Water Science Center – Sentinel Island station
[f]USGS Nevada Water Science Center – Boulder Basin station
[g]Bureau of Reclamation – Lower Colorado Office
[h]Based on processed MABEL data with respect to WGS84 Ellipsoid
[i]With respect to EGM96 Geoid
[j]NOAA Chesapeake Bay Interpretive Buoy System
[k]Depth at which $LSBR_0$ first reaches 0.
[l]Estimated as four times the water surface standard deviation
[m]Mean number of photons in atmosphere per meter depth per meter horizontal transect
[n]Mean number of detected water surface photons per meter of flight transect
[p]Average of *in situ* upswelling and downswelling radiance attenuation measure by NOAA STAR team

Because both the total observed return and the mean background can be computed directly from the observed vertical profile, and because the background can range over several orders of magnitude, Equation 1 is more conveniently rewritten as

$$LSBR(d) = Log_{10}\left[\frac{\rho_L(d) + \rho_{SB} + \rho_{LB} + \rho_{DC}}{\rho_{SB} + \rho_{LB} + \rho_{DC}} - 1\right] \quad (2)$$

where the numerator in the brackets represents the total return observed by MABEL including both signal and background photons. Prior to computing *LSBR(d),* a vertical histogram of the total return is created at 0.05-m bin increments using all water photons observed along the flight path. The mean background in the denominator is estimated from observed atmospheric photons. *LSBR(d)* is computed and smoothed employing a 0.5- to 1.0-m moving average as necessary depending on the specific site.

RESULTS

The current analysis examines three MABEL datasets of coastal and inland water observed during 2012 to 2013, focusing on along track surface water height, light penetration into water under a range of atmospheric and water conditions, and near-shore bottom topography. Sites include the middle Chesapeake Bay, the near-shore Atlantic Ocean coast at Virginia Beach, and Lake Mead.

Site 1: Middle Chesapeake Bay

The two Chesapeake Bay transects are shown in Figure 4. They represent contrasting day and night open water cases with moderate wind and turbidity with mostly clear sky conditions. Both transects consist of a one-minute acquisition along nearly identical 8-km reaches in the middle of the bay near NOAA's Gooses Reef buoy. The September 22, 2012, flight occurred during late evening local time and the September 25, 2013, flight during midday local time. There were no land crossings and water depth was greater than 10 m.

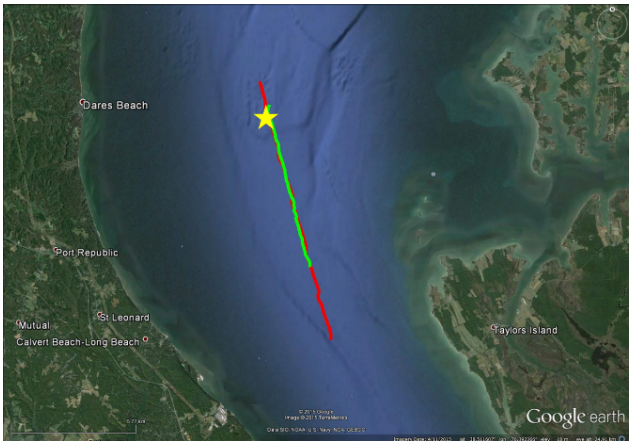

Figure 4. Location map of high-altitude MABEL flights over Site 1 in both 2012 (green line) and 2013 (red line) on Chesapeake Bay near Gooses Reef buoy. Base map from Google Earth.

Plots of the georeferenced MABEL photon cloud returns from the atmosphere through the water column with respect to the WGS84 Geodetic height are shown in Figures 5a and b. The plots consist primarily of i) background photons throughout the atmosphere and water column, ii) a concentrated band of photons of about a meter wide representing the water surface, and iii) an additional band of subsurface backscattered photons extending a few meters below the water surface and diminishing with depth. The above profiles are typical of most MABEL water transects.

The plots indicate notable differences in background rates, surface signal photon rates, and SBR penetration between the two dates. The 2012 late evening flight exhibits an almost negligible background rate of 0.00002 m^{-2} for this nighttime flight. The 2013 midday flight, however, exhibits variable background along the flight line, shown in Figure 5b and in an expanded view in Figure 6, with a moderate background rate of 0.011 m^{-2} between a distance of 2,000 and 4,300 m, followed by a low background rate of 0.0053 m^{-2} over the distance 4,300–6,300 m. The different backgrounds for the same 2013 transect

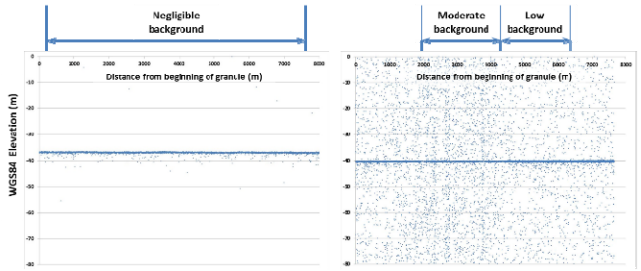

Figure 5. Along track profile of MABEL-observed photons for Site 1 during the 2012 (a) and 2013 (b) flights on Chesapeake Bay near Gooses Reef.

represent differences in cloud cover within the instrument field of view. Clouds increase the solar scattering while reducing the lidar surface signal.

Analysis also indicates that for the 2013 Chesapeake cases, that occurred during daytime within a minute of each other, nearly four times as many water surface photons were detected, or 2.20 m^{-1} versus 0.56 m^{-1}, in the low background segment compared to the moderate segment, respectively. As indicated in Figure 5b, however, the moderate background segment still easily possesses sufficient photons to clearly define the water surface.

The *LSBR(d)* profiles of the Chesapeake cases, shown in Figure 7, indicate the observable limits of MABEL's subsurface volume scattering. Results indicate that the *LSBR(d)* profile for 2013 decays faster for the moderate background segment compared to the low background 2013 case. The observable penetration of both 2013 cases is less than the 2012 Chesapeake case, indicating greater observability at night when there is no solar background.

For quantitative comparison of the observable MABEL penetration, it is useful to choose a threshold level, say $LSBR_0$, representing the depth at which the signal-to-noise ratio equals one or $Log_{10}(SBR)$ equals 0. Results shown in Table 2 and Figures 6 and 7 indicate that $LSBR_0$ equals 1.3 m and 3.7 m for the 2013 moderate and low backgrounds, respectively, despite having the same turbidity of 2.9 NTU. As defined, MABEL's observable $LSBR_0$ depth is not only a function of the intrinsic properties of the water but also the relative intensity of the incident signal photons compared to the background. Lower background makes it easier to discern a given signal strength. For the 2012 late evening case, this observable depth or $LSBR_0$ equals 6.8 m, a much deeper depth, resulting largely from the very low background.

Once $LSBR_0$ is defined, the attenuation of the MABEL subsurface backscattered signal can be explored and modeled as an exponential decay with depth. The water penetration of a 532-nm laser beam has been shown to decrease exponentially proportional to the diffuse attenuation coefficient (Guenther, 1985; Feygels *et al.*, 2003). MABEL analyses yielded attenuation coefficients of α_{532} = 0.91 m^{-1} (R^2 = 0.53) and 0.56 m^{-1} (R^2 = 0.84) for the moderate and low background cases, respectively. Lower R^2 generally occurs with the smaller $LSBR_0$

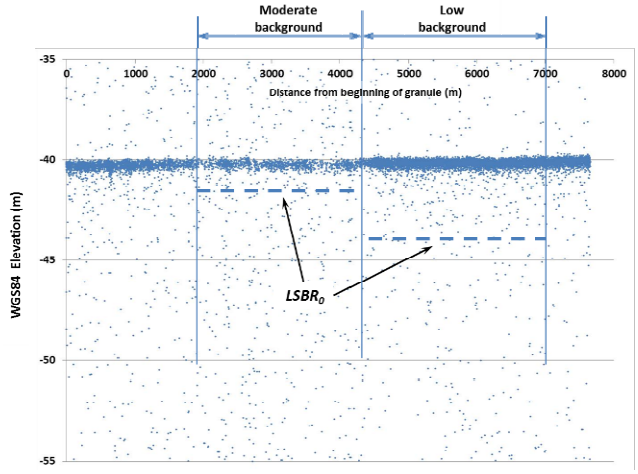

Figure 6. Expanded view of MABEL 2013 data at site 1, Chesapeake Bay near Gooses Reef buoy. Results also indicate SBR_{10} depths of –1.3 m and –3.7 m for moderate (0.011m^{-2}) and low (0.0053m^{-2}) background, respectively, for the same turbidity of 2.9 NTU.

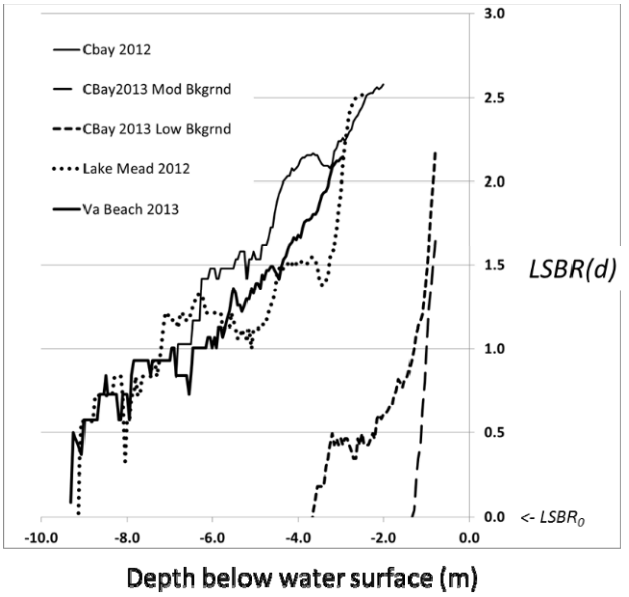

Figure 7. Signal to background ratio profiles versus depth, *LSBR(d),* for five cases presented in this study, expressed in Log_{10} base. Also indicated is the $LSBR_0$ threshold level.

depth as there are fewer data to fit the subsurface decay. *In situ* measurements of diffuse solar light at 532.2 nm were also made along the 2013 transect using a free falling HyperPro II by Satlantic. Data were averaged over three casts for each location. The mean of the upwelling and downwelling diffuse attenuation coefficients were K_{532} = 0.45 m^{-1} (R^2 = 0.99) and 0.52 m^{-1} (R^2 = 0.99) for the moderate and low background cases, respectively.

The estimated MABEL-based attenuation is thus slightly higher with a lower R^2 than the *in situ* results. Error sources include difference in instrumentation, spatial variability in water turbidity over the length of the transect, and some differences in the precise time of acquisition.

Site 2: Atlantic Ocean near Virginia Beach

The second site analyzed was an east-west transect extending from the Atlantic Coast at Virginia Beach, just south of the mouth of the Chesapeake, eastward into the Atlantic on September 19, 2013, at 22:30 UTC (late afternoon local time). Figure 8 shows the transect location map, which is situated just south of the mouth of the Chesapeake Bay. A 20-second segment of about 2,000 MABEL photons is plotted in Figure 9. For this date, sky conditions were mostly clear, and the wind was from the east at 4.2 m/s. One additional feature not seen in the Chesapeake Bay cases is evidence of some wave structure throughout the transect. This is attributed to the MABEL flight being aligned nearly parallel to the wind direction.

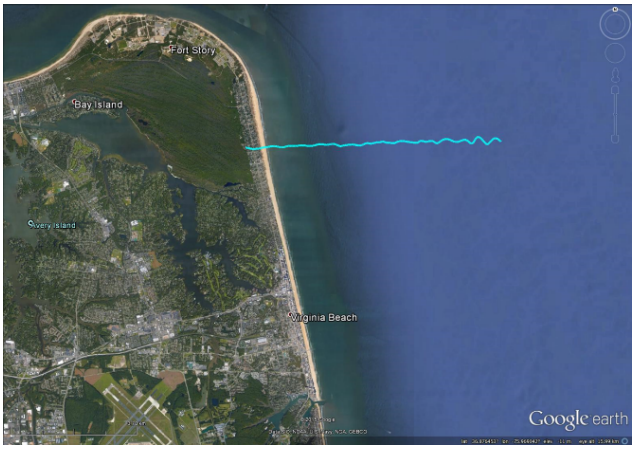

Figure 8. Location map of high-altitude MABEL flights over Site 2, Atlantic Ocean near Virginia Beach. Base map from Google Earth.

Also plotted on Figure 9 is the $LSBR_0$ depth estimated to be about 9.3 m. This comparatively high penetration is attributed to a combination of the lower turbidity of 2.2 NTU compared to the Chesapeake Bay cases, and a low background rate of 0.0003 m^{-2}. The attenuation coefficient is estimated to be $\alpha_{532} = 0.55\ m^{-1}$ ($R^2 = 0.95$).

Furthermore, although a distinct bottom is not identified even near the shore, evidence of an approximate implied bottom may be possible when there is a sharp drop in LSBR. Drawn on Figure 9 is an estimated envelope of MABEL's subsurface signal photons in the vicinity of the shore. The envelope suggests that the water depth extends down to about 4 m at a distance of about 200 m from shore. Although precise measurements of bathymetry were not recorded at the time of the MABEL flight, the depth of the envelope curve is consistent with current bathymetric soundings available from the National

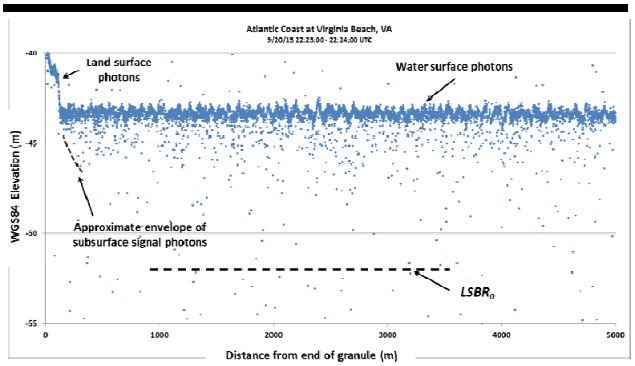

Figure 9. Along track profile of MABEL-observed photons for Site 2, Atlantic Coast at Virginia Beach. $LSBR_0$ depth indicated at 9.3 m below surface. Estimated envelope of near shore subsurface signal photons suggests approximate location of bottom.

Ocean Service Hydrographic Data Base, NOAA National Centers for Environmental Information (https://www.ngdc.noaa.gov/mgg/bathymetry/hydro.html).

A vertical histogram of the water surface height computed from the aggregated along track MABEL photon elevations is shown in Figure 10. Photon heights are plotted with respect to the WGS84 Ellipsoid. Orthometric heights using the EGM96 Geoid are also provided in Table 1. This histogram does not represent the true statistical distribution of the surface photons as the effect of the instrument impulse response is convolved with the returned signal. The ICESat-2 ATL13 Inland Water Height Data Product algorithm deconvolves the MABEL signal,

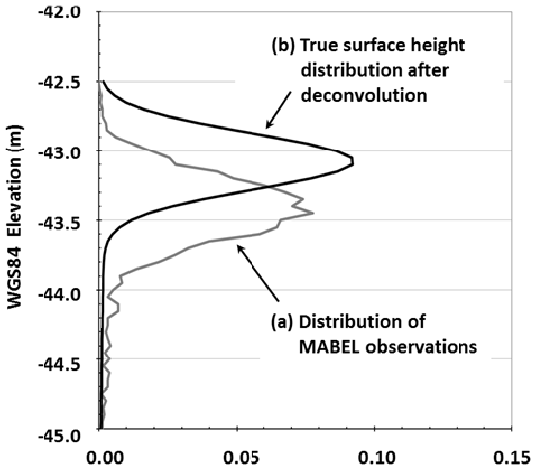

Figure 10. Histograms of the water surface photons for Site 2, Atlantic Ocean at Virginia Beach, for (a) the MABEL observations and (b) the estimated true surface distribution after deconvolution.

providing an estimate of the true representation of the distribution of the surface variability also shown in Figure 10. The estimated true water surface height distribution for the Site 2 case yields a standard deviation of 0.21 m and an offset of about 0.30 m in the mode from the MABEL observations.

Site 3: Lake Mead

This case represents a night flight over a relatively clear water body with turbidity equal to 1.6 NTU. The MABEL overpass of February 24, 2012, transected the western portion of Lake Mead in a southwest to northeast direction as shown in Figure 11. The transect represents two granules of data, or about 2 minutes of acquisition, covering about 24 km.

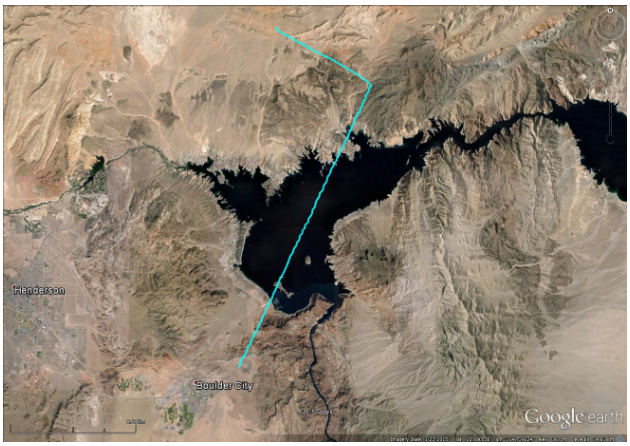

Figure 11. Location map of high-altitude MABEL flights over Site 3, Lake Mead. Base map from Google Earth.

The corresponding plot of the MABEL photons is shown in Figure 12, with the southwestern corner of the lake on the left. During the flight approximately 91,000 photons were recorded. Because of the nighttime and clear sky conditions, there was an extremely low background count of 0.00008 m^{-2}. Several features are clearly identified. First, starting at the edge of the lake and traversing across, several islands are noted. To the far right of the figure, after passing over a large island nearly 60 m high, the aircraft reaches the edge of the lake. Subsurface backscatter results in an estimated $LSBR_0$ depth of 9.2 m. The attenuation coefficient is estimated to be α_{532} = 0.37 m^{-1} (R^2 = 0.73).

Unlike the previous cases, the bathymetry of Lake Mead is very apparent in the vicinity of many of the shorelines of the lake edges and islands. To see this more clearly, an expanded view of the photons is plotted in Figure 13 for the southwest shore. Prior to plotting, data were first processed to remove an instrument after pulse at about 1.4 m depth. The near-shore bottom of the lake is observed as an extension of the shoreline to a depth of nearly 9 m. The corresponding histograms of the surface and subsurface photons are shown for an open water

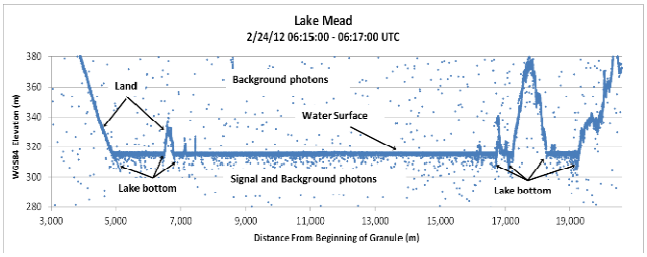

Figure 12. Along track profile of water body and near-shore MABEL-observed photons for Site 3, Lake Mead, on February 24, 2012, 6:15-17 UTC.

stretch of 2 km in Figure 14a and a near-shore stretch of 100 m in Figure 14b. In the open water segment, the water depth is much greater than the $LSBR_0$ depth of 9.2 m and no bottom signal is detected. For the near-shore profile, a bottom bump in the histogram is clearly identified at about a depth of 2 m. Although a detailed map is not available, these results are consistent with the NOAA Nautical Chart 18687 of the National Ocean Service Coast Survey (http://www.oceangrafix.com/chart/zoom?chart=18687).

DISCUSSION

The five different cases over three sites presented here cover a range of atmospheric and water states for evaluating the high-altitude prototype MABEL system. From the perspective of water surface height profiling, several parameters were computed for each case including background rate, rate of detected water surface signal photons, $LSBR_0$, water surface height standard deviation, and vertical height precision, and the MABEL subsurface attenuation coefficient. These parameters, summarized in Table 2, provide insight on what photon counting can offer in inland and near-shore water bodies as well as the anticipated performance of ICESat-2.

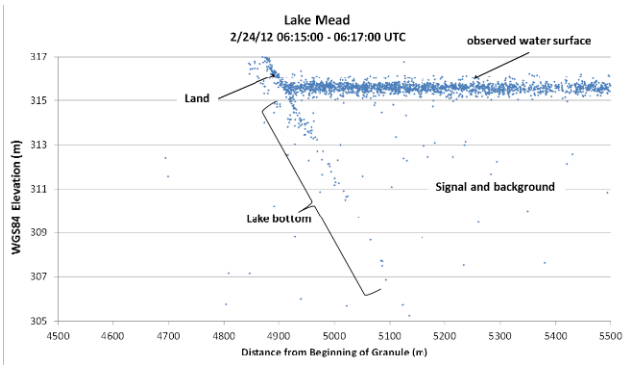

Figure 13. Expanded view of MABEL observations at land water crossing of Lake Mead on the southwest shore. Results show penetration of the 532-nm channel into the water column and the presence of lake bottom along the western edge, up to a depth of about 10 m.

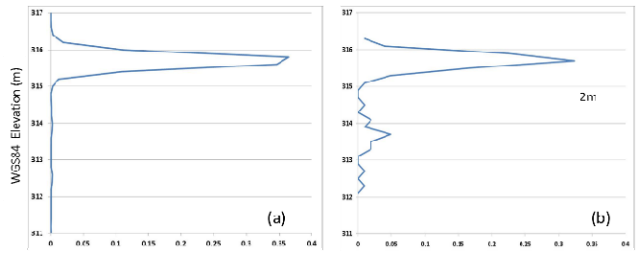

Figure 14. Histograms of MABEL data for (a) a deep, open water 2-km stretch near the center of the Lake Mead, and (b) a near-shore 100-m stretch near southwestern Lake Mead. Typical bump in near-shore histogram indicates lake depth of about 2 m.

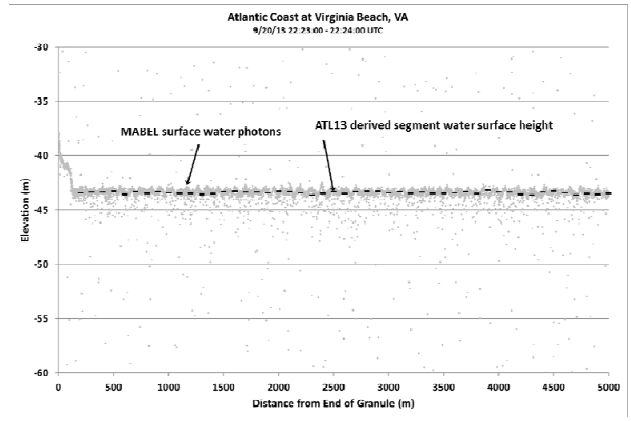

Figure 15. Same as Figure 9 with the addition of the approximate ATL13 data product consisting of aggregated (100 photons) water surface height segments for Site 2, Atlantic Coast at Virginia Beach.

For instance, the mean signal rate is critical to evaluating measurement precision of the ICESat-2 Inland Water Height data product. For the present analysis, water surface photons detection ranged from 0.36 m^{-1} over the Chesapeake Bay in 2012 to 2.9 m^{-1} over Lake Mead during 2012. Although the lower return rates are generally associated with clouds and haze, some of the low rates may have been associated with low MABEL pulse energy for the different flights.

For the Virginia Beach case, mean heights of water surface photons have been aggregated in approximately 100-m segments, as shown in Figure 15. Given its water signal rate of 0.41 m^{-1} and assuming a vertical precision of 30 cm/photon (personal communication, Thomas Neumann, ICESat-2 Project Office), the approximate vertical precision of each 100-m segment can be estimated as

$$Precision\ of\ 100m\ segment = \frac{30}{\sqrt{water\ signal\ rate * 100m}} \quad (3)$$

or 4.7 cm. Using the water signal photon rate from Table 2 for the other cases, the estimated vertical precision ranges from about 1.8 cm over Lake Mead where signal density is highest to 5.0 cm for the 2012 Chesapeake Bay flight where density is lowest. Other factors associated with instrument pulse strength, orbit pointing, and atmospheric delays may alter the error of an additional few percent.

Additional important relationships are related to the standard deviation of wave height, σ_h, such as the significant wave height, $H_{1/3}$, that represents the mean wave height (trough to crest) of the highest third of the waves. Computation of MABEL's along track surface photon height standard deviation, σ_h, ranged from 0.065 m for the September 2013 flight to 0.21 m for the September 2013 Virginia Beach case. A plot of the *in situ* significant wave height reported using NOAA buoy data, versus the mean standard deviation of water height calculated from the MABEL data, is shown in Figure 16. The slope yields the relationship, $H_{1/3} = 4.79\ \sigma_h$, only slightly higher than the generally accepted value of 4.0 used to estimate the significant wave height (Holthuijsen, 2007). No corrections to possible observation bias were made.

From the perspective of MABEL use for bathymetry, only the Lake Mead case, which had the lowest turbidity of 1.6 NTU, showed a definitive bottom signal in multiple near-shore locations. The solar background was also the lowest at 0.0003 m^{-2}, yielding a $LSBR_0$ depth of 9.2 m. Analysis of the current datasets indicates no global relation between SNR and turbidity across all the case studies. Examination of other Chesapeake datasets, however, not presented herein, yielded other examples of near-shore examples of bottom topography, however, they were not as clear as the Lake Mead case. The results confirm the difficulty of observing bathymetry in the narrow, near-shore

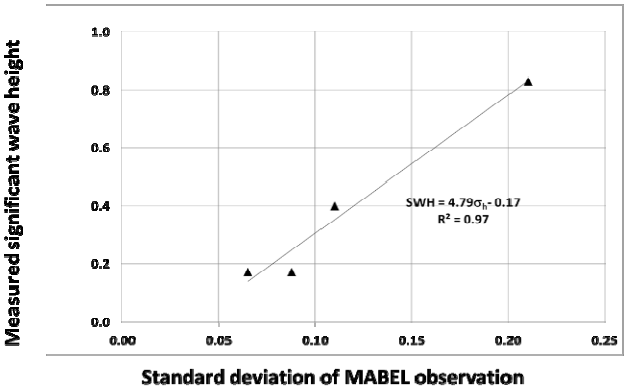

Figure 16. *In situ* NOAA buoy significant wave height, $H_{1/3}$, versus MABEL observed water surface height standard deviation, σ_h, for Chesapeake Bay and Virginia Beach cases. Fitted slope yields $H_{1/3} = 4.79\sigma_h$, only slightly higher than the generally accepted value of 4.0 used in the definition of significant wave height.

shallow zone using low-energy photon counting systems. Practical future use of ICESat2 for mapping bathymetry is thus best achieved for clear water bodies, up to several NTUs, and only along the prescribed satellite reference tracks.

Finally, in analogy to the often used relation between the Secchi Disk Depth (SDD) and Photosynthetically active

Radiation (PAR) attenuation or SDD x K_{par} = constant (Poole and Atkins, 1929), it can be shown using the MABEL findings in Table 2 that

$$LSBR_0 \times \alpha_{532} = 3.3 \quad (4)$$

Although not equivalent, the analogous results fall within the reasonable range of 1.7 to 4.95 reported by Gallegos, Werdell, and McClain (2011).

CONCLUSIONS

MABEL was designed as a high-altitude prototype of the ICESat-2 ATLAS sensor; therefore, the results presented here can be expected to be similar to those retrieved from space. The analyses of five datasets over the three near-shore MABEL experiment sites thus provide an opportunity to understand the performance of the anticipated ICESat-2/ATLAS mission and the viability of global inland and coastal surface water height data product. The ICESat-2 project will implement a calibration/validation plan during the project life cycle, and performance will be periodically reviewed. The plan will include targeting additional high latitude lakes not analyzed here.

Analysis of the high-altitude MABEL observations using the ATL13 Inland Water Height Data Product algorithms demonstrated the capability of retrieving along track mean and standard deviation of water surface height under clear and partly cloudy conditions. Such height products would be especially beneficial in remote global regions not easily accessible by aircraft. ICESat-2's low repeat coverage in the low and mid latitudes during its first two years after launch, however, would limit its use in many operational applications. Higher latitude regions would benefit to a great degree due to a combination of close reference track and cross over analysis.

A simple method for determining the observable penetration of the 532-nm beam has been defined in terms of the SBR(d) penetration profile. The $LSBR_0$ is a useful parameter for estimating the range of observable depth over which attenuation can be modeled. The capability to observe bottom signals has been shown to be feasible, but only under the most favorable atmospheric and water optical conditions.

While additional research is required, the overall results suggest that the retrieval of surface water height statistics from space-based photon counting systems such as ATLAS is very high for resolutions down to about 100 m, even in partly cloudy conditions. Mean water surface height precisions of approximately 5–10 cm per 100-m segment length may be achievable.

For the subsurface, the results indicate that the low energy MABEL system can profile up to about one Secchi disc depth (SDD) under clear skies. For homogeneous water body surfaces, deeper penetrations may be achieved by analyzing longer flight segments of several hundred meters or more.

ACKNOWLEDGMENTS

This work was supported by the NASA Cryosphere Program through the ICESat-2 Project Office, and also the Goddard Space Flight Center Strategic Support. We acknowledge the MABEL instrument and flight support team including Eugenia DeMarco, Dan Reed, and the ICESat-2 project scientists including Thorsten Markus and Thomas Neumann, the advice provided by David Harding of GSFC's Planetary Geodynamics Laboratory. Figures 1 and 2 were provided by the ICESat-2 Project Office. We are especially grateful to the NOAA NESDIS Center for Satellite Applications and Research for conducting the 2013 field experiment in the Chesapeake Bay, and also two anonymous reviewers whose careful review and suggestions substantially improved the manuscript.

LITERATURE CITED

Abdalati, W.; Zwally, H.; Bindschadler, R.; Csatho, B.; Farrell, S.; Fricker, H.; Harding, D.; Kwok, R.; Lefsky, M.; Markus, T.; Marshak, A.; Neumann, T.; Palm, S.; Schutz, B.; Smith, B.; Spinhirne, J., and Webb, C., 2010. The ICESat-2 Laser Altimetry Mission. *Proceedings of the Institute of Electrical and Electronics Engineers*, 98(5), 735–751.

Abshire, J.B.; Sun, X.; Riris, H.; Sirota, J.M.; McGarry, J.F.; Palm, S.; Yi, D., and Liiva, P., 2005. Geoscience Laser Altimeter System (GLAS) on the ICESat Mission: On-orbit measurement performance. *Geophysical Research Letters*, 32, L21S02, doi:10.1029/2005GL024028.

Ackermann, F., 1999. Airborne laser scanning—present status and future expectations. *Journal of Photogrammetry and Remote Sensing*, 54, 64–67.

Barrick, D.E., 1968. Rough surface scattering based on the specular point theory. *Institute of Electrical and Electronics Engineers Transactions on Antenna and Propagation*, AP-16, 449–454.

Barton, J. and Jasinski, M., 2011. Sensitivity of depth-integrated satellite lidar to subaqueous scattering. *Remote Sensing,* 3, 1492–1515. doi:10.3390/rs3071492.

Birkett, C.M.; Reynolds, C.; Beckley, B., and Doorn, B., 2011. From Research to Operations: The USDA Global Reservoir and Lake Monitor, Chapter 2. *In*: Vignudelli, S.; Kostianoy, A.G.; Cipollini, P., and Benveniste J. (eds.), *Coastal Altimetry*. Berlin: Springer-Verlag, pp. 19–50.

Bonisteel, J.M.; Nayegandhi, A.; Wright, C.W.; Brock, J.C., and Nagle, D.B., 2009. *Experimental Advanced Airborne Research lidar (EAARL) Data Processing Manual*. *U.S. Geological Survey Open-File Report 2009–1078*, 38p.

Brock, J.C. and Purkis, S.J., 2009. The emerging role of lidar remote sensing in coastal research and resource management. *In:* Brock, J.C. and Purkis, S.J. (eds.), *Coastal Applications of Airborne Lidar*. *Journal of Coastal Research*, Special Issue No. 53, pp. 1–5.

Bufton, J.L.; Hoge, F.E., and Swift, R.N., 1983. Airborne measurements of laser backscatter from the ocean surface. *Applied Optics*, 22, 2603–2618.

Calmant, S.; Seyler, F., and Cretaux, J.-F., 2008. Monitoring continental surface waters by satellite altimetry. *Survey in Geophysics*, 29, 247−269, doi:10.1007/s10712-008-9051-1.

Churnside, J., Naugolnykh, K., and Marchbanks, R., 2014. Optical remote sensing of sound in the ocean. *Journal of Applied Remote Sensing*, 9, doi:10.1117/1.JRS.9.096038.

Dabney, P.; Harding, D.; Abshire, J.; Huss, T.; Jodor, G.; Machan, R.; Marzouk, R.; Rush, K.; Seas, A.; Shuman, C.; Sun X.; Valett, S.; Vasilyev, A.; Yu, A., and Zheng, Y., 2010. The slope imaging multi-polarization photon-counting lidar:

development and performance results. *Institute of Electrical and Electronics Engineers International Geoscience and Remote Sensing Symposium (IGARSS)* (Honolulu, HI), doi:10.1109/IGARSS.2010.5650862.

Degnan, J.; Machan, R.; Leventhal, E.; Jodor, G.; Field, C., and Sirota, J.M., 2011. Cryosphere and biomass measurements using a photon-counting 3D imaging lidar. *Conference on Lasers and Electro-Optics (CLEO)* (Baltimore, MD), pp. 1–2.

Estep, L.L.; Lillycrop, W.J., and Parson, L.E., 1994. Estimation of maximum depth of penetration of a bathymetric lidar system using a Secchi depth data base. *Marine Technology Society Journal*, 28, 31–36.

Feygels, V.; Park, J.; Aitken, J.; Kim, M.; Payment, A., and Ramnath, V., 2012. Coastal Zone Mapping and Imaging Lidar (CZMIL): first flights and system validation. *SPIE Vol. 8532: Remote sensing of the ocean, sea ice, coastal waters, and large water regions 2012* (Edinburgh, U.K.), doi:10.1117/12.2014617.

Feygels, V.; Wright, C.W.; Kopilevich, Y., and Surkov. A., 2003. Narrow-field-of-view bathymetrical lidar: theory and field test. *SPIE 5155: Ocean Remote Sensing and Imaging II* (San Diego, CA), doi:10.1117/12.506951.

Fuchs, E. and Mathur, A., 2010. Utilizing circular scanning in the CZMIL system. *SPIE Proceedings Vol. 7695: Algorithms and Technologies for Multispectral, Hyperspectral, and Ultraspectral Imagery XVI* (Baltimore, MD), doi:10.1117/12.851936.

Gallegos, C.; Werdell, P., and McClain, C., 2011. Long-term changes in light scattering in Chesapeake Bay inferred from Secchi depth, light attenuation, and remote sensing measurements. *Journal Geophysical Res,* C00H08, doi:10.1029/2011JC007160, 2011.

Guenther, G.C., 1985. *Airborne Laser Hydrography: System design and performance factors*. Rockville, MD: National Ocean Service, NOAA Professional Paper Series, 396p.

Guenther, G.; LaRocque, P., and Lillycrop,W., 1994. Multiple surface channels in SHOALS airborne lidar. *In*: Jaffe, J.S. (ed.), *Ocean Optics* XII, *International Society for Optics and Photonics Proceedings* (location), pp. 422–430.

Guenther, G.C.; Tomas, R.W.L., and LaRocque., P.E., 1996. Design considerations for achieving high accuracy with the SHOALS bathymetric lidar system. *In*: Feigels, V.I. and Kopilevich, Y.I. (eds.), *Laser Remote Sensing of Natural Waters: From Theory to Practice. International Society for Optics and Photonics Proceedings,* pp. 54–71.

Guenther, G., 2007. Airborne lidar bathymetry digital elevation: model technologies and applications. *In*: Maune, D. (ed.), *The DEM Users Manual, 2nd edition*. Bethesda, Maryland: American Society for Photogrammetry and Remote Sensing, pp. 253–320.

Harding, D. and Jasinski M.J., 2004. ICESat observations of inland surface water stage, slope, and extent: A new method for hydrologic monitoring. *American Geophysical Fall Meeting* (San Francisco, California).

Harding, D.; Dabney, P.; Valett, S.; Yu, A.; Vasilyev, A., and Kelly, A., 2011. Airborne polarimetric, two-color laser altimeter measurements of lake ice cover: A pathfinder for NASA's ICESat-2 spaceflight mission. *Institute of Electrical and Electronics Engineers International Geoscience Remote Sensing Symposium (IGARSS)* (Vancouver, BC, Canada), 3598–3601, doi:10.1109/IGARSS.2011.6050002.

Holthuijsen, L.H., 2007. *Waves in Oceanic And Coastal Waters.* Cambridge: Cambridge University Press, 70p.

Hu, Y.; Stamnes, K.; Vaughan, M.; Pelon, J.; Weimer, C.; Wu, D.; Cisewski, M.; Sun, W.; Yang, P.; Lin, B.; Omar, A.; Flittner, D.; Hostetler, C.; Trepte, C.; Winker, D.; Gibson, G., and Santa-Maria, M., 2008. Sea surface wind speed estimation from space-based lidar measurements. *Atmospheric Chemistry and Physics*, 8, 3593–3601, doi:10.5194/acp-8-3593-2008.

Irish, J.L. and Lillycrop, W.J., 1999. Scanning laser mapping of the coastal zone: the SHOALS system. *Journal of Photogrammetry and Remote Sensing*, 54(1999), 123–129.

Jasinski, M.; Harding, D.; Neumann, T.; McGill, M.; Martino, T.; Cook, B., and Brunt, K., 2013. Overview: MABEL and Simulated ATLAS Data Products, *ICESat-2 Applications Workshop, March 10-11, 2015*, Greenbelt, MD. https://www.signup4.net/Public/ap.aspx?EID=TEMP455E.

Klemas, V., 2011. Beach profiling and lidar bathymetry: an overview with case studies. *Journal of Coastal Research*, 27(6), 1019–1028.

Krabill, W.B.; Abdalati, W.; Frederick, E.B.; Manizade, S.S.; Martin, C.F.; Sonntag, J.G.; Swift, R.N.; Thomas, R.H., and Yungel, J.G., 2002. Aircraft laser altimetry measurement of elevation changes of the Greenland ice sheet: Technique and accuracy assessment. *Journal of Geodynamics,* 34, 357–376, doi:10.1016/S0264-3707(02)00040-6.

Krainak, M.; Yang, G.; Lu, W., and Sun, X., 2010. Photon-counting detectors for space-based applications. *International Society for Optics and Photonics, Conference on Detectors and Imaging Devices - Infrared, Focal Plane, Single Photon* (San Diego, California), doi:10.1117/12.864025.

Lancaster, R.S.; Spinhirne, J.D., and Palm, S.P., 2005. Laser pulse reflectance of the ocean surface from the GLAS satellite lidar. *Geophysical Research Letters,* 32, L22S10, doi:10.1029/2005GL023732.

Lillycrop, W.J.; Irish, J.L., and Parson, L.E., 1997. SHOALS System. *Sea Technology,* 38,17–25.

Lillycrop, W.J.; Pope, R.W., and Wozencraft, J.M., 2002. Airborne lidar hydrography: A vision for tomorrow. *Sea Technology,* 43(6), 27–34.

McGill, M.J.; Hlavka, D.L.; Hart, W.D.; Scott, V.S.; Spinhirne, J.D., and Schmid, B., 2002. Cloud physics lidar: Instrument description and initial measurement results. *Applied Optics*, 41, 3725–3734.

McGill, M.; Markus, T.; Scott, V.S., and Neumann, T., 2013. The Multiple Altimeter Beam Experimental Lidar (MABEL): An airborne simulator for the ICESat-2 mission. *Journal of Atmospheric and Oceanic Technology*, 30, 345–352. doi: 10.1175/JTECH-D-12-00076.1.

McKean, J.; Nagel, D.; Tonina, D.; Bailey, P.; Wright, C.W.; Bohn, C., and Nayegandhi, A., 2009. Remote sensing of channels and riparian zones with a narrow-beam aquatic-terrestrial lidar. *Remote Sensing*, 1(4), 1065–1096.

Menzies, R.T.; Tratt, D.M., and Hunt, W.H., 1998. Lidar In-space Technology Experiment measurements of sea surface directional reflectance and the link to surface wind speed. *Applied Optics,* 37, 5550–5559.

National Research Council, 2007. *Earth Science and Applications from Space: National Imperatives for the Next Decade and Beyond*. Washington, DC: National Academy Press, 428p.

Nayegandhi, A.; Brock J.C., and Wright, C.W., 2009. Small-footprint, waveform-resolving lidar estimation of submerged and sub-canopy topography in coastal environments. *International Journal of Remote Sensing,* 30, 861–878.

Pan, Z.; Glennie, C.; Hartzell, P.; Fernandez-Diaz, J.; Legleiter, C., and Overstreet, B., 2015. Performance assessment of high resolution airborne full waveform LiDAR for shallow river bathymetry. *Remote Sensing,* 7, 5133–5159; doi:10.3390/rs70505133.

Parrish, C.E.; Jeong, I.; Nowak, R.D., and Smith, R.B., 2011. Empirical comparison of full-waveform lidar algorithms: range extraction and discrimination performance. *Photogrammetric Engineering & Remote Sensing,* 77(8), 825–838.

Pfennigbauer, M.; Ullrich, A.; Steinbacher, F., and Aufleger, M., 2011. High-resolution hydrographic airborne laser scanner for surveying inland waters and shallow coastal zones. *Proc. SPIE 8037, Laser Radar Technology and Applications*, 11p.

Poole, H.H. and Atkins, W.R.G., 1929. Photoelectric measurements of submarine illumination throughout the year. *Journal of the Marine Biological Association of the United Kingdom,* 16, 297–324, doi:10.1017/S0025315400029829.

Schutz, B.E.; Zwally, H.J.; Shuman, C.A.; Hancock, D., and DiMarzio, J.P., 2005. Overview of the ICESat Mission. *Geophysical Research Letters*, 32, L21S01, doi:10.1029/2005GL024009.

Schroeder, D.J., 1999. *Astronomical Optics (2nd ed.).* San Diego, CA, Academic Press, 478p.

Sinclair, M. and Penley, M., 2007. Processing lidar data for charting applications – Understanding the trade-offs and challenges. *US Hydro 2007* (Norfolk, VA).

Sinclair, M., 1999. Laser hydrography – commercial survey operations. *Proceedings, US Hydrographic Conference '99*. (Mobile, Alabama, USA).

Sinclair, M., 2008. Airborne lidar hydrographic survey for homeland security. *Sea Technology*, 49(3), 15–20.

Spinhirne, J.D., 1993. Micro pulse lidar. *Institute of Electrical and Electronics Engineers Transactions on Geoscience and Remote Sensing*, 31(1), 48–55.

Tulldahl, H.M. and Wikström, S., 2012. Classification of aquatic macrovegetation and substrates with airborne lidar. *Remote Sens. Environ.* 121, 347–357. doi:10.1016/j.rse.2012.02.004.

U.S. Department of Commerce, 2002. NOAA National Ocean Service Coast Survey, Chart 18687, 13th Ed.

White, S.A.; Parrish, C.E.; Calder, B.R.; Pe'eri, S., and Rzhanov, Y., 2011. Lidar-derived national shoreline: empirical and stochastic uncertainty analyses. *In:* Pe'eri, S. and Long, B. (eds.), Applied LIDAR Techniques. *Journal of Coastal Research*, Special Issue No. 62, pp. 62–74.

Wright, C.W.; Fredericks, X.; Troche, R.J.; Klipp, E.S.; Kranenburg, C.J., and Nagle, D.B., 2014. *EAARL-B coastal topography–Eastern New Jersey, Hurricane Sandy, 2012; first surface (version 1.1, August 18, 2014). U.S. Geological Survey Data Series 767*, http://dx.doi.org/10.3133/ds767.

Wright, C.W. and Brock, J.C., 2002. EAARL: A LiDAR for mapping shallow coral reefs and other coastal environments. *Proceedings of the 7th International Conference on Remote Sensing for Marine and Coastal Environments* (Miami, FL), (CD-ROM).

Zhang G.; Xie, H.; Kang S.; Yi, D., and Ackley, S.F., 2011a. Monitoring lake level changes on the Tibetan Plateau using ICESat altimetry data (2003–2009). *Remote Sensing of the Environment*, 115, 1733–42.

Zhang, G.; Xie, H.; Duan, S.; Tian, M., and Yi, D., 2011b. Water level variation of Lake Qinghai from satellite and in situ measurements under climate change. *Journal of Applied Remote Sensing*, 5(1), 053532, doi.10.1117/1.3601363.

Zwally, H.J.; Li, J.; Brenner, A.; Beckley, M.; Cornejo, H.; DiMarzio, J.; Giovinetto, M.; Neumann, T.; Robbins., J.; Saba., J.; Yi, D., and Wang, W., 2011. Greenland ice sheet mass balance: Distribution of increased mass loss with climate warming; 2003-07 versus 1992-02. *Journal of Glaciology*, 57, 88–102.